DOI：10. 13471/j. cnki. acta. snus. ZR20230041

Photochemical synthesis of ultrafine platinum nanocatalysts and their application in the catalytic reduction of nitrophenols*

XIAN Liang[1,2]✉, *TIAN Xiaoxia*[1], *MA Jing*[1], *LI Wei*[1]

1. *School of Chemical Engineering, Northwest Minzu University, Lanzhou 730030 , China*
2. *Key Laboratory for Utility of Environment-Friendly Composites and Biomass in Universities of Gansu Province, Lanzhou 730030, China*

Abstract: This study focuses on synthesizing ultrafine platinum nanoparticles (Pt/C_{60}-E) by irradiating a mixture of C_{60} and $K_2[PtCl_4]$ with ethylene glycol (EG) as the reducing agent. The process utilizes near-ultraviolet (UV) light at a wavelength of 395 nm, along with visible light at 450 and 650 nm. The composition and morphology of the Pt/C_{60} catalyst were investigated using characterization techniques including X-ray diffraction (XRD), Fourier transform infrared spectroscopy (FT-IR), X-ray photoelectron spectroscopy (XPS), and high-resolution transmission electron microscopy (HR-TEM). The results revealed a well-dispersed distribution of Pt nanoparticles on the C_{60} surface, with an average particle size of about 2.6 nm. In the catalytic reduction experiments of *p*-NP, the Pt/C_{60}-E3 catalyst, prepared under near-ultraviolet irradiation (395 nm), exhibited superior catalytic activity, with a rate constant (k) of 0.12 min^{-1}. Furthermore, in the catalyst cycling experiments, the catalysts remained highly active even after multiple cycles, demonstrating the effectiveness of the photochemical method in synthesizing precursor Pt catalysts.

Key words: platinum ultrafine nanoparticles; fullerene; photochemical method; degradation of *p*-nitrophenol

CLC number: O643　　**Document code:** A　　**Article ID:** 2097－0137（2024）03－0137－10

The versatile optical, electrical, and electronic properties of metallic nanoparticles have led to their widespread applications in the fields of sensing, biomedicine, electronics, imaging, and particularly in catalysis in recent years (Chang et al. , 2014). The catalytic efficiency of nanomaterials is primarily controlled by factors such as size, shape, concentration, and temperature (Song , 2022). Among these factors, the size of metal particles plays a crucial role in regulating the catalytic activity of loaded nanocatalysts. Noble metal nanocatalysts are usually loaded with nanoscale or sub-nanoscale metal particles onto carrier materials that possess a high specific surface area, which improves catalytic activity.

As a precious metal, Pt is widely used as an efficient catalyst for chemical reactions, but its high price and scarce reserves have limited industrial development. An effective solution to this challenge is to research and develop high-performance and low-cost Pt nanocatalysts (Mao et al. , 2016). Generally, the catalytic activity of Pt nanoparticles (NPs) increases with smaller size and a higher number of

* **Received**: 2023－12－17　　**Accepted**: 2024－01－24　　**Published online**: 2024－03－21
Supported by National Natural Science Foundation of China（52167003）;
Key Research and Development Projects in Gansu Province（21YF5WA064）

✉ **Corresponding author**: XIAN Liang（*lxian@xbmu.edu.cn*）
TIAN Xiaoxia（*1726905151@qq.com*）; MA Jing（*849879969@qq.com*）; LI Wei（*1747015656@qq.com*）

surface atoms. However, the high surface energy of small-sized Pt nanoparticles tends to cause agglomeration, which can lead to decreased catalytic activity. Therefore, to prevent Pt agglomeration, strategies such as using surface-bound ligands, creating core-shell or alloy nanostructures, and using chemical deposition have been implemented. These approaches stabilize noble metal nanoparticles, leading to highly dispersed and stable catalysts (Xiang et al. , 2011; Guo et al. , 2012; Xie et al. , 2012; Din et al. , 2020; Zhao et al. , 2020; Gan et al. , 2021; Ortiz-Herrera et al. , 2022; Zhang et al. , 2023a).

Among various carriers, carbon-based materials are particularly effective in enhancing the dispersion and activity of catalysts. These include activated carbon, porous carbon, carbon nanotubes, and fullerenes (Shi et al. , 2019; Zhou et al. , 2020; Yoo et al. , 2022; Sun et al. , 2022; Li et al. , 2023; Yang et al. , 2023). In particular, C_{60} has been used as a new type of catalyst carrier due to its unique properties, including large specific surface area, porosity, corrosion resistance, high electronic and thermal conductivity, special mechanical properties, and high electrochemical stability (Lee et al. , 2009). The results showed that the addition of C_{60} had a significant effect on the final morphology of the nanoparticles, leading to more uniform dispersion as the C_{60} content increased (Bhardwaj et al. , 2017).

Conventionally, Pt nanocatalysts have been prepared using various methods, including chemical reduction, impregnation, microwave-assisted, atomic layer deposition, and photochemical reduction (Swain et al. , 2022). Among these methods, photochemical reduction stands out as a simple, clean, and eco-friendly approach. It initiates electron transitions in metal ions through light irradiation, causing them to react with reducing agents and form metal nanoparticles. Additionally, this method allows indirect control over the reduction kinetics of $K_2[PtCl_4]$ by adjusting the wavelength range, illumination duration, and light intensity.

With the aid of light (such as visible and near-ultraviolet light), the reduction of platinum ions can be efficiently achieved using ethylene glycol (EG), which contains multiple hydroxyl groups. The interaction between EG and the precursor facilitates better control over the average particle size of the metal nanoparticles (Jiang et al. , 2005; Santiago et al. , 2007; de Bortoli et al. , 2023). In this experiment, Pt UPs loaded on C_{60} (Pt/C_{60}-E) were synthesized by irradiating a mixed solution of C_{60} and $K_2[PtCl_4]$ precursor with near-ultraviolet and two wavelengths of visible light, using EG as the reducing agent. The composition, content, and morphology of the Pt/C_{60} catalysts were investigated using XRD, FT-IR, XPS, EDS, TEM, and HR-TEM techniques. Additionally, the catalytic efficiency of Pt/C_{60} was evaluated through the catalytic degradation of *p*-NP.

1 Experimental

1. 1 Materials

Potassium chloroplatinate ($K_2[PtCl_4]$, ≥98%) was purchased from China Aladdin Biochemical Science and Technology Co. ,Ltd. ; fullerene (C_{60}, 99. 5%) was purchased from Bailing Wei Science and Technology Co. ,Ltd. ; concentrated nitric acid (HNO_3) and concentrated sulfuric acid (H_2SO_4) were purchased from Sichuan Xilong Chemical Co. , Ltd. ; *p*-nitrophenol (*p*-NP, ≥ 99%) was purchased from Tianjin Tianxin Fine Chemical Development Center; sodium borohydride ($NaBH_4$) was purchased from Shanghai Zhongqin Chemical Reagent Co. , Ltd. ; ethylene glycol (EG) was purchased from Sinopharm Group Chemical Reagent Co. , Ltd. LED lamp (12 W, 6 500 K); UV lamp (12 W, model E27). The solutions used in the experimental process were prepared with Milli-Q ultrapure water (18. 2 MΩ·cm), and all the reagents were analytically pure and could be used directly without further purification.

1. 2 Preparation of Pt/C_{60}-E

1. 2. 1 Pre-treatment of C_{60} Weigh 0. 075 g of C_{60} in a 250 mL conical flask, add 45 mL of concentrated sulfuric acid, and ultrasonic under the condition of ice water bath for 30 min to obtain the brown suspension. Subsequently, 15 mL of deionized water and 15 mL of concentrated sulfuric acid were added while stirring, and the system was warmed up to 90 ℃ and then refluxed in a water bath for 4 h to form a clear

and transparent brown solution.

After the brown solution was cooled to room temperature, 2 mol/L NaOH solution was added, and the pH was adjusted to above 9. At this time, a large amount of insoluble suspension appeared in the solution, which was left overnight to make the insoluble material fully precipitated, and the precipitate was separated by centrifugation and washed repeatedly with methanol to pH=7, and the brown powder product was obtained after drying.

1.2.2 Preparation of Pt/C_{60}-E Weigh 8 mg of pretreated C_{60}, add it to 30 mL of EG solution, and sonicate for 30 min to form a C_{60} suspension. Under light-avoiding conditions, 30 mL of K_2 [$PtCl_4$] solution (2 mmol/L) was added dropwise into the C_{60} suspension stirring while dropping. Subsequently, the reaction was illuminated with blue-violet (LED fluorescent lamp plus filter at 450 nm) light and magnetically stirred for 4 h. The suspension was separated by centrifugation and washed several times with deionized water, and the black solid particles were collected after drying and labeled as Pt/C_{60}-E1.

Under the same conditions, the light condition was changed to a red lamp (LED fluorescent lamp plus a filter with a wavelength of 650 nm) for continuous irradiation and magnetic stirring reaction for 4 h, and the prepared sample was labeled Pt/C_{60}-E2. The light condition was changed to the near-ultraviolet lamp (wavelength 395 nm) for continuous irradiation and magnetic stirring reaction for 4 h, and the obtained sample was labeled Pt/C_{60}-E3.

1.3 Characterization of Pt/C_{60}-E

FT-IR was performed on a Satellite 5 000 infrared spectrometer with a wave number range of 4 000 ~ 1 000 cm^{-1}. UV-Vis was performed on a UV-1200 UV spectrophotometer. The elemental composition of the samples was characterized on an XPS Kratos AXIS Ultra DLD with an Al Kα lamp as the excitation source and the C1*s* peak (at 284.8 eV) was used as an internal reference for the absolute binding energy of the XPS peak. Finally, XPS Peak software is used for spectral analysis and data processing. XRD patterns of the samples were obtained using an ARL XTRA X-ray diffractometer (Switzerland) with Cu Kα-rays as the radiation source over an angular range of 10° ~ 90° (2θ) at a rate of 2°/min and were analyzed by XRD-MDI Jade 6. Transmission electron microscopy (TEM, JEM 2100 Jeol (Japan) characterized the catalysts' morphology and distribution. Before the TEM test, the samples were mixed with ethanol and then sonicated before being dropped on micro sand and air-dried at room temperature. The samples' SEM images and energy dispersive X-ray (EDS) spectra were obtained by EVO18 scanning electron microscopy.

1.4 Catalytic Performance Experiment

The catalytic performance of the prepared Pt/C_{60}-E catalysts was evaluated by catalytic reduction of *p*-NP at room temperature in the presence of $NaBH_4$ excess. First, 5 mL of a 0.2 mmol/L *p*-NP solution was mixed with 5 mL of a freshly prepared 10 mmol/L $NaBH_4$ solution. Subsequently, 2 mg of the catalyst was added to this mixture. The supernatant was taken every 2 min and the peak change of UV-Vis absorption spectrum at 275 ~ 500 nm was monitored. After the reaction was completed, the sample was separated via centrifugation, collecting the solid particles at the bottom. These particles were washed several times with deionized water, air-dried, and then subjected to cyclic stability testing.

2 Results and discussion

2.1 XRD characterization

Fig. 1(a) and (b) show the XRD patterns of Pt/C_{60}-E1, Pt/C_{60}-E2, and Pt/C_{60}-E3. Both C_{60} and Pt metal diffraction peaks appeared in the XRD pattern of Pt/C_{60}-E, indicating the successful preparation of the Pt/C_{60}-E sample and the successful loading of the carrier with Pt^0 metal. Fig. 1(b) Diffraction peaks at 2θ of 10.8°, 17.7°, and 20.8° can be attributed to the (002), (101), and (102) facets in C_{60} (Tol et al., 2005); five peaks at 39.8°, 46.3°, 66.8°, 81.9°, and 86.1° are the characteristic peaks of the face-centered-cubic (*fcc*) crystals Pt, which are distributed at (111), (200), (220), (311) and (222) facets (Tuo et al., 2018). Compared to Pt/C_{60}-1 (Xian et al., 2022), the Pt characteristic peaks are significantly higher, and the sharp diffraction peaks in the XRD pattern of Pt/C_{60}-E3

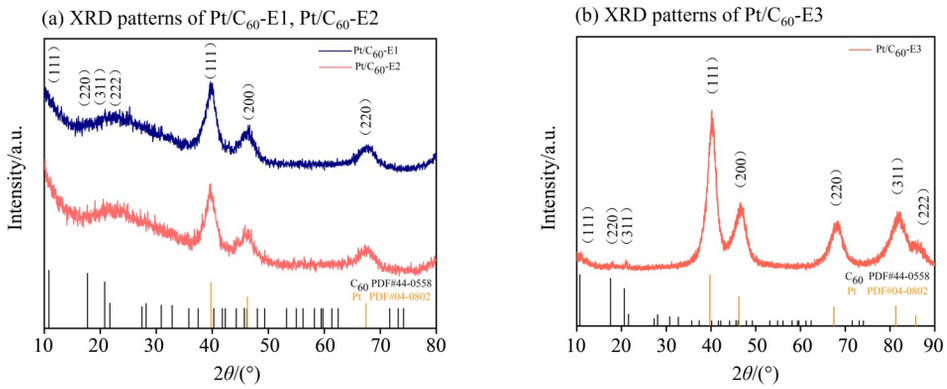

Fig. 1 XRD patterns of the sample

indicate that the generated platinum metal has good crystallinity and the Pt Ups loaded on the surface of the carriers are present in smaller sizes (Shi et al. , 2016; Li et al. , 2017).

The average grain size of Pt in Pt/C_{60}-E was calculated using the following Scherrer equation1 (Xue et al. , 2019)

$$D = k\lambda/(\beta\cos\theta)\ , \qquad (1)$$

D: average crystal size, k: Scherrer's constant (0. 89), λ: X-ray wavelength (0. 154 06 nm), β: half-peak width in radians, θ: diffraction angle. The average particle sizes of Pt/C_{60}-E1, Pt/C_{60}-E2, and Pt/C_{60}-E3 were deduced from the half peak width of the Bragg peak to be 3. 1, 3. 48, and 2. 5 nm, respectively, and the size of the Pt/C_{60}-E3 sample was smaller than that of the other two samples, which indicates that near-ultraviolet light is more suitable for the preparation of ultrathin platinum nanoparticles than the other two kinds of light in the experimental conditions.

2. 2 TEM characterization

Fig. 2 shows the transmission electron microscopy (TEM) image and the histogram of the grain size distribution of Pt/C_{60}-E3, which can clearly and intuitively observe the microscopic morphology and distribution of Pt UPs. Fig. 2(a) HR-TEM results show that the grain spacing is 0. 23 nm, which is related to the (111) plane of Pt. This result is in agreement with the above XRD results and was able to confirm the presence of Pt nanoparticles on the carrier surface (Cho et al. , 2008). From Fig. 2(b), it can be seen that the Pt/C_{60}-E3 catalysts all exhibit a low degree of agglomeration, and the slight agglomeration may be attributed to the occurrence of platinum autocatalytic reaction around the platinum grains, which results in the formation of an inhomogeneous morphology of the surface distribution. By measuring the particle size of more than 200 particles in Fig. 2(c), the average particle size of the nanoparticles was calculated to be (2. 6±0. 1) nm, and the particle sizes obtained by TEM were slightly larger than the values of the grain sizes obtained by XRD. Since XRD only measures grain size, the discrepancy could be caused by a slight agglomeration of the Pt UPs, which is reflected by the TEM grain size. However, the values obtained by the two algorithms show similar results and agree with each other to a large extent. These results clearly show that the Pt Ups are uniformly distributed on C_{60},

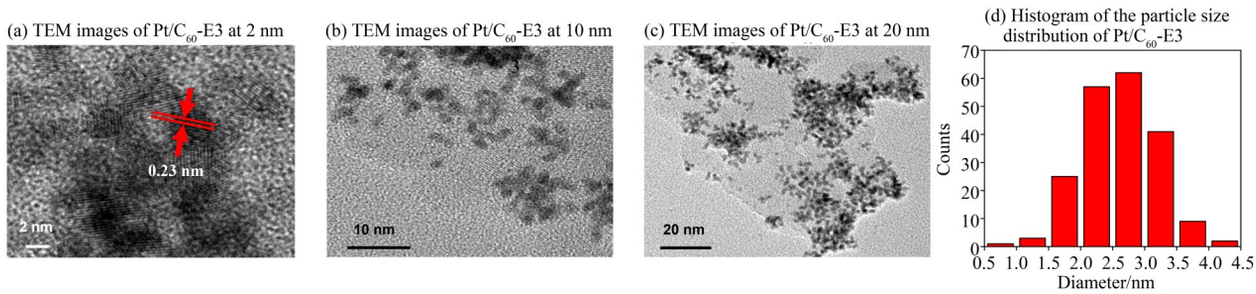

Fig. 2 TEM images and histogram of the particle size distribution of Pt/C_{60}-E3

with a notably small size. Under experimental conditions using near-UV and visible light as sources, the $K_2[PtCl_4]$ precursor solution changed from orange to black after 4 hours of irradiation. This color change indicated the reduction of $[PtCl_4]^{2-}$ in the aqueous EG solution and the formation of black Pt metal in the presence of light (Xian et al. , 2022).

In analyzing the mechanisms behind Pt nanoparticles' formation, it's noted that C_{60}, being semiconductor-like, can facilitate the diffusion of photogenerated electrons on its surface. This suggests the presence of photogenerated electron-reduced platinum complexes in the system. Alcohol reduction is also a factor, attributed to the presence of EG in the reaction solution. Under light exposure, Pt complexes are first excited. These excited complexes then react with alcohol molecules to form free radical complexes, which are subsequently reduced to elemental platinum Pt^0 (Ma et al. , 2013).

2. 3 SEM and EDS characterization

Elemental measurements were carried out to investigate the presence and distribution of Pt, O, and C in the Pt/C_{60}-E3 composite. Fig. 3(a) shows the SEM image of Pt/C_{60}-E3, and Fig. 3(b-d) shows the elemental C, O, and Pt face-scan EDS maps of Pt/C_{60}-E3. It can be seen that elements C (Fig. 3(b)) and Pt (Fig. 3(d)) are well distributed on the surface of the composite material, indicating the existence of Pt UPs on the surface of C_{60} and the successful preparation of Pt/C_{60}-E3 composite material. The Pt content is 40. 6% (wt), which is higher than that of Pt/C_{60}-1 (Xian et al. , 2022), indicating that more platinum was reduced in the presence of EG.

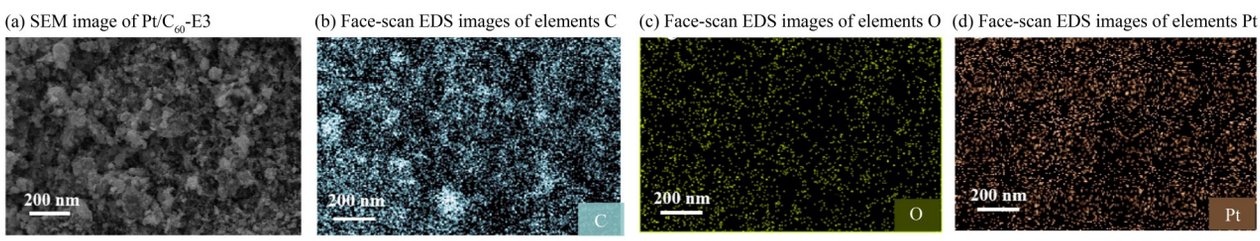

Fig. 3 SEM image and face-scan EDS images of elements of Pt/C_{60}-E3

2. 4 FT-IR characterization

Fig. 4 shows the FT-IR spectra of purified C_{60} and Pt/C_{60}-E1, Pt/C_{60}-E2, and Pt/C_{60}-E3. The IR absorption peaks at 3 439 and 3 448 cm^{-1} correspond to the —OH stretching vibration in the interlayer water molecules (Zhu et al. , 2008). The peaks at 2 918 cm^{-1}, as well as 2 920 cm^{-1}, are C-H stretching vibrations. The peak at 2 356 cm^{-1} is a characteristic CO_2 peak, which may be formed due to the adsorption of CO_2 molecules by the material during the testing process (Fang et al. , 2006). The absorption peaks at 1 627 and 1 626 cm^{-1}, as well as at 1 108 and 1 103 cm^{-1}, correspond to the telescopic vibrations of the C═O groups in carboxyl and the C—O groups. In addition, the peaks at 1 366, and 1 375 cm^{-1} are due to the torsional vibration of the O—H bond (Subhan et al. , 2021). These results indicate that the obtained C_{60} was modified by oxygen-containing groups such as —OH and C═O through acid oxidation. Furthermore, the synthesis techniques, such as ultrasound used in producing Pt/C_{60}-E3, did not alter the original structure of the C_{60} carrier. It can be seen from Figure 4 that Pt/C_{60}-E3 has a small shift compared to the peak position of C_{60}, which may be caused by the interaction of Pt ions with functional groups on C_{60}.

2. 5 XPS characterization

To further confirm the formation of Pt/C_{60}-E3, its chemical composition and valence state were investigated using XPS spectroscopy. Fig. 5(a) shows the complete XPS spectrum of Pt/C_{60}-E3. The binding energy peaks at 284. 8, 531. 2, and 71. 2 eV are the chemical binding energies of C1*s*, O1*s*, Pt4*d*, and Pt4*f* states, respectively (Zhao et al. , 2005), revealing the presence of C, O, and Pt elements. The C1*s* XPS spectrum of C_{60} is shown in Fig. 5(b), and the peaks of the fitted curves are 284. 8, 286. 6, and 288. 5 eV, respectively. These peaks correspond to the functional groups C—C, C—O, and C═O. As mentioned

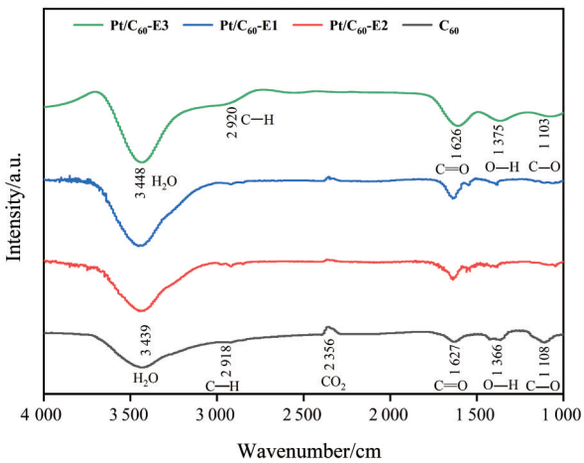

Fig. 4 FT-IR spectra of C_{60} and Pt/C_{60}-E1, Pt/C_{60}-E2 and Pt/C_{60}-E3

above, the oxygen-containing functional groups bound on the surface of carbon carriers play an important role in the deposition of Pt, which may be the nucleation site of Pt Ups (Nie et al. , 2012).

Fig. 5(c) represents the binding energy spectra of the Pt 4*f* region of the studied Pt/C_{60}-E3 catalysts, with spin-orbit splitting of Pt $4f_{7/2}$ and $4f_{5/2}$ at binding energies of 71. 0 and 74. 4 eV, respectively. The bimodal can be decomposed into three components: Pt^0 in the metallic state, and Pt^{2+} and Pt^{4+} in their respective oxidized states. The fitted peaks of Pt in the Pt/C_{60}-E3 catalyst at 71. 3 and 74. 5 eV correspond to the characteristic peaks of Pt^0 $4f_{7/2}$ and Pt^0 $4f_{5/2}$, at 72. 6 and 75. 6 eV correspond to the characteristic peaks of Pt^{2+} $4f_{7/2}$ and Pt^{2+} $4f_{5/2}$, and at 75. 0 and 78. 1 eV correspond to the characteristic peaks of Pt^{4+} $4f_{7/2}$ and Pt^{4+} $4f_{5/2}$ characteristic peaks (An et al. , 2002). From the figure, it can be seen that the intensity of the XPS characteristic peak corresponding to Pt^0 is higher, indicating that EG enhances the conversion of Pt^{2+} and Pt^{4+} to Pt^0. This observation aligns with the findings from the XRD analysis. In addition, a small portion of Pt^{2+} still exists as PtO or $Pt(OH)_2$, and a small portion of Pt^{2+} is oxidized to Pt^{4+} by air and exists as PtO_2 (Kertalli et al. , 2017; Ismail et al. , 2021).

2. 6 Catalyzing the degradation of *p*-NP

2. 6. 1 Effect of different wavelengths on catalyst performance

The catalytic degradation of *p*-NP to *p*-AP was monitored by UV-Vis spectrophotometry,

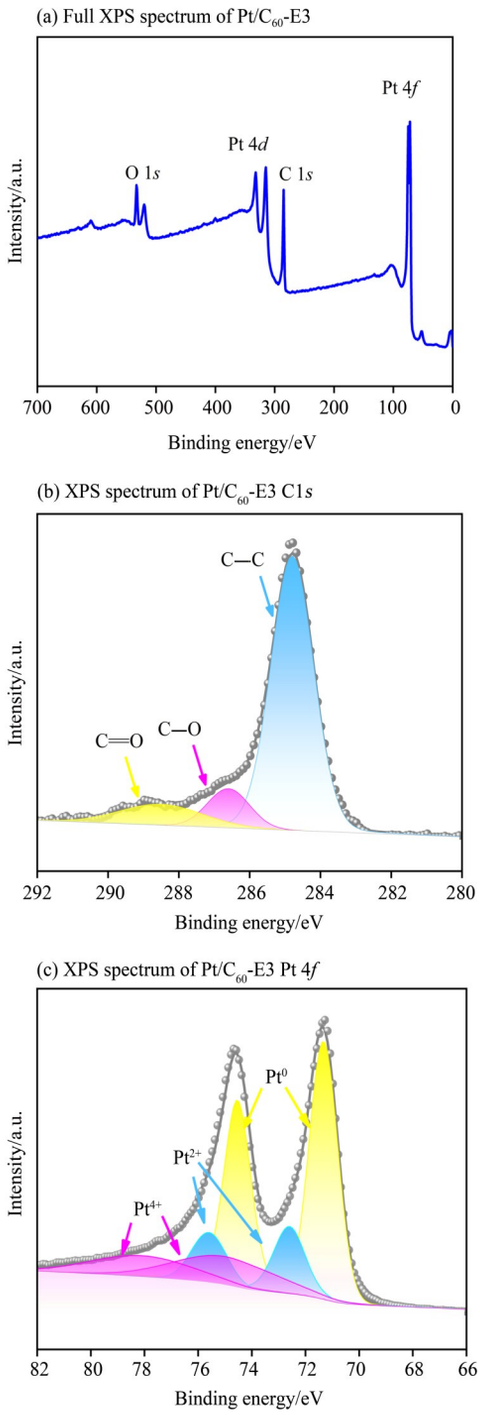

Fig. 5 XPS spectrum of Pt/C_{60}-E3

and the UV spectral range was maintained at 275 ~ 400 nm. In the aqueous phase, *p*-NP is light yellow, displaying a strong absorption peak at 317 nm in the UV-Vis spectrum. Upon the addition of $NaBH_4$, the solution turns bright yellow, and the peak shifts from 317 to 400 nm, indicative of the formation of the *p*-nitrophenolate anion (Dai et al. , 2016). Upon addition of Pt/C_{60} UPs to the *p*-NP reaction solution,

Pt/C_{60}-E3 reduced the *p*-NP dye to *p*-AP within 18 min, with a rapid decrease in the absorption spectrum at 400 nm (shown in Fig. 6a). The spectra of the catalytic degradation of *p*-NP by Pt/C_{60}-E1 and Pt/C_{60}-E2 are shown in Fig. 6(c,d). During the conversion of *p*-NP to *p*-AP, Pt UPs facilitate the rapid transfer of electrons from the nucleophilic BH_4^- to the electrophilic *p*-NP molecules (Bathula et al. , 2020; Zhang et al. , 2023b). To understand the reaction kinetics of catalytic reduction of *p*-NP, the catalytic reaction rate was quantitatively analyzed. The absorbance ratio of A_t/A_0 and the reaction time (t) were plotted on a negative logarithmic scale, and linear fitting was applied to the relevant data in Fig. 6(a). The pseudo-first-order kinetic diagrams calculated by the rate constants of Pt/C_{60}-E1, Pt/C_{60}-E2, and Pt/C_{60}-E3 obtained from the rate equation $\ln(A_t/A_0) = -kt$ are shown in Fig. 6(b). The k-value of Pt/C_{60}-E3 was 0. 12 min^{-1}, whereas the k-values of Pt/C_{60}-E1 and Pt/C_{60}-E2 were 0. 10 and 0. 08 min^{-1}, respectively. These results indicate that Pt/C_{60}-E3 is more active and faster than Pt/C_{60}-E1 and Pt/C_{60}-E2 in *p*-NP catalytic reduction in water.

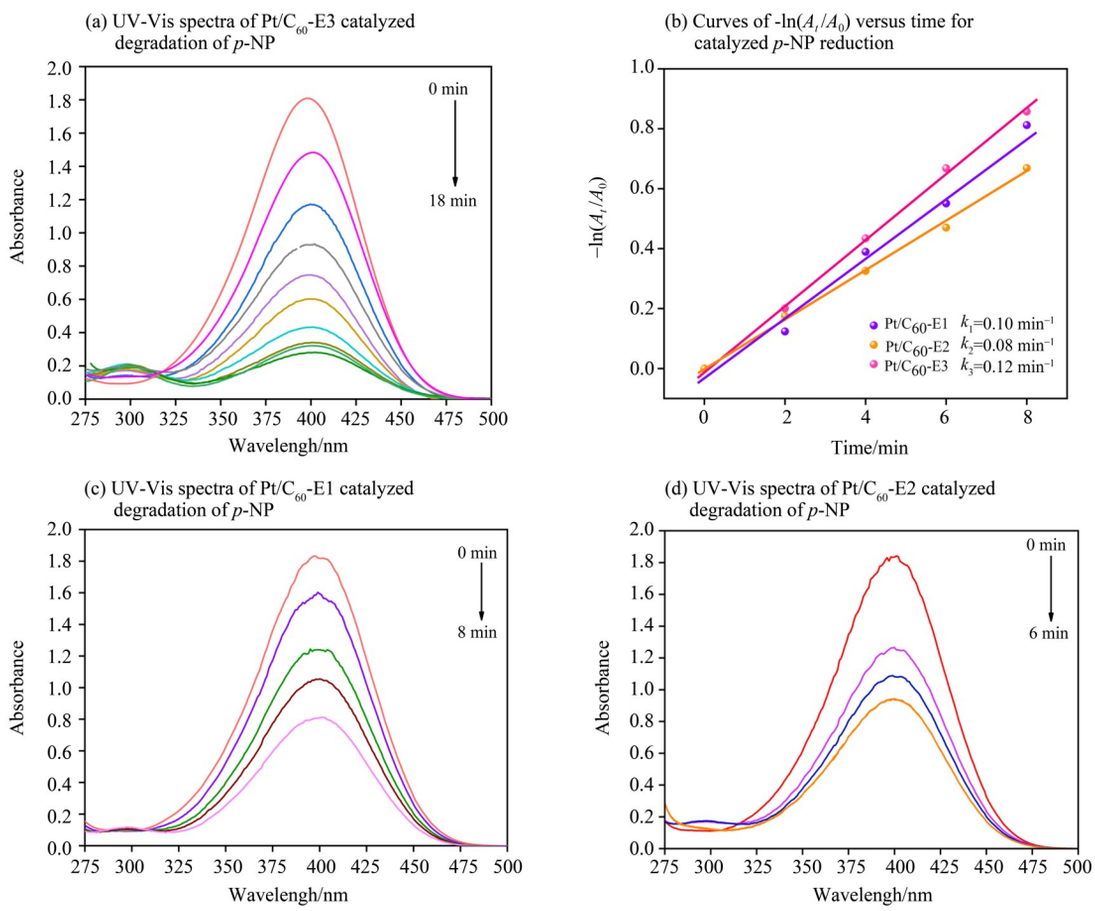

Fig. 6 Degradation and reduction of *p*-NP

In the precursor $K_2[PtCl_4]$ solution, the hydrolysis products of $[PtCl_4]^{2-}$ and the hydrolysis rate affect the dynamic nucleation and growth of metal atoms, which in turn affect the distribution and morphology of metal nanoparticles. Different wavelengths of light irradiation can influence the rate of hydrolysis and the distribution of its products. Generally, shorter wavelengths result in faster hydrolysis rates (Liu et al. , 2016; Xian et al. , 2021). Therefore, it can be concluded that when using EG as a reducing agent, near-UV irradiation accelerates the hydrolysis rate of $K_2[PtCl_4]$. This results in a more favorable formation of Pt^0, leading to an increased reaction rate. The k values of Pt/C_{60}-E3, as demonstrated in this experiment, were compared with various other catalysts documented in the literature, as shown in Table 1. These comparisons show that the Pt/C_{60}-E3 prepared in this experiment has good catalytic reduction activity.

Table 1 The magnitude of k values of different catalysts for catalytic p-NP reduction at room temperature

Catalyst	Catalyst addition /mg	Concentration of p-NP /(mol·L^{-1})	k/min^{-1}	References
Pt/C_{60}-E3	2. 0	2. 0×10^{-4}	0. 12	This work
Au	6. 0	1. 0×10^{-4}	0. 02	Panigrahi et al. ,2007
RGO-$Ni_{25}Co_{75}$	6. 0	5. 0×10^{-3}	0. 093	Bai et al. ,2012
Ag NPs	2. 0	3. 0×10^{-4}	0. 003	Li et al. ,2015
Hydrazine-free copper anowires	0. 02	2. 0×10^{-4}	0. 075	Ranjana et al. , 2023

2. 6. 2 Measurement of cyclic stability

Catalytic stability is an important characteristic of nanocatalysts for practical applications. To assess the catalytic stability of Pt/C_{60} nanocatalysts, the representative Pt/C_{60}-E3 nanocatalyst was chosen for multiple cycle tests in the reduction of p-NP by $NaBH_4$. Fig. 7 shows that the conversion rate marginally decreases with each additional cycle. The observed decrease in catalyst performance may be attributed to two factors: the agglomeration of Pt nanoparticles during cycling experiments (Zhou et al. , 2023), and potential loss of the catalyst due to the inefficient recovery of small-sized Pt nanoparticles during centrifugation. The conversion of the original catalyst was still maintained at 86% in the 7th cycle, and the results confirmed the high catalytic stability of the prepared Pt/C_{60}-E3 nanocatalysts.

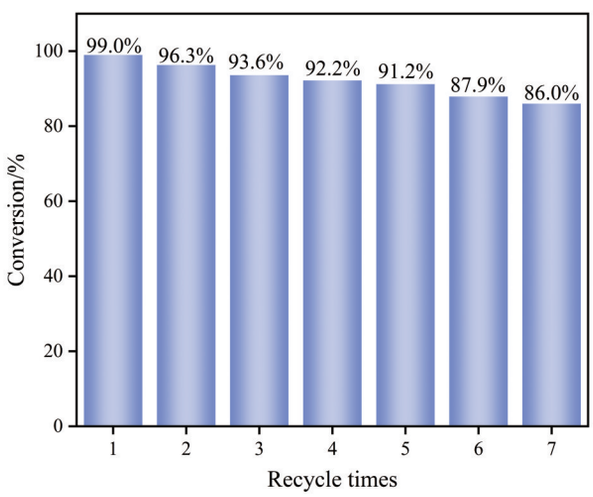

Fig. 7 Reusability of Pt/C_{60}-E3 nanocatalysts for catalytic reduction of p-NP

3 Conclusions

In this experiment, uniformly dispersed platinum nanocatalysts (Pt/C_{60}-E) were synthesized on C_{60} using a photochemically assisted ethylene glycol (EG) reduction method. The elemental composition and morphology of the Pt/C_{60}-E3 sample were analyzed using various techniques, including XRD, FT-IR, XPS, EDS, SEM, and TEM tests. The results showed that the Pt UPs were uniformly distributed on the C_{60} surface, with the Pt/C_{60}-E3 catalysts having an average particle size of (2. 6±0. 1) nm. In subsequent experiments for the catalytic reduction of p-NP, the rate constants (k) for the three catalyst samples were determined to be 0. 08, 0. 05, and 0. 12 min^{-1}, respectively. Among the catalysts, Pt/C_{60}-E3, prepared under near-ultraviolet (395 nm) conditions, exhibited high catalytic activity in the reduction of p-NP. It maintained a stable conversion efficiency of about 86% even after seven consecutive reaction cycles, indicating good stability in aqueous solutions. This experiment offers valuable insights into the study of platinum nanocatalysts supported by visible light.

References:

AN W, CHUANG K T, SANGER A R, 2002. Catalyst-support interaction in fluorinated carbon-supported Pt catalysts for reaction of NO with NH_3[J]. J Catal, 211(2): 308-315.

BAI S, SHEN X, ZHU G, et al, 2012. *In situ* growth of Ni_xCo_{100-x} nanoparticles on reduced graphene oxide nanosheets and their magnetic and Catalytic Properties[J]. ACS Appl Mater Interfaces, 4(5): 2378-2386.

BATHULA C, SUBALAKSHMI K, KUMAR K A, et al, 2020. Ultrasonically driven green synthesis of palladium nanoparticles by *Coleus amboinicus* for catalytic reduction and Suzuki-Miyaura reaction[J]. Colloids Surf B Biointerfaces, 192: 111026.

BHARDWAJ A, KAUR J, WUEST M, et al, 2017. In situ click chemistry generation of cyclooxygenase-2 inhibitors [J]. Nat Commun, 8(1): 1-9.

CHANG J, FENG L, LIU C, et al, 2014. Ni_2P enhances the activity and durability of the Pt anode catalyst in direct methanol fuel cells [J]. Energy Environ Sci, 7(5): 1628-1632.

CHO Y H, YOO S J, CHO Y H, et al, 2008. Enhanced performance and improved interfacial properties of polymer electrolyte membrane fuel cells fabricated using sputter-deposited Pt thin layers [J]. Electrochim Acta, 53(21): 6111-6116.

DAI Y, YU P, ZHANG X, et al, 2016. Gold nanoparticles stabilized by amphiphilic hyperbranched polymers for catalytic reduction of 4-nitrophenol[J]. J Catal, 337: 65-71.

de BORTOLI A L, 2023. Flow simulation in direct ethanol fuel cells using multifunctional anode catalysts[J]. J Power Sources, 560: 232675.

DIN I U, SHAHARUN M S, NAEEM A, et al, 2020. Carbon nanofibers as potential materials for catalysts support, a mini-review on recent advances and future perspective[J]. Ceram Int, 46(11): 18446-18452.

FANG Q R, ZHU G S, JIN Z, et al, 2006. A multifunctional metal-organic open framework with a bcu topology constructed from undecanuclear clusters[J]. Angew Chem Int Ed Engl, 45(37): 6126-6130.

GAN J, HUANG Z, LUO W, et al, 2021. Platelet carbon nanofibers as support of Pt-CoO electrocatalyst for superior hydrogen evolution[J]. J Energy Chem, 52: 33-40.

GUO X F, JANG D Y, JANG H G, et al, 2012. Hydrogenation and dehydrogenation reactions catalyzed by CNTs supported palladium catalysts[J]. Catal Today, 186(1): 109-114.

ISMAIL A A, ALBUKHARI S M, MAHMOUD M H H, 2021. Highly efficient and accelerated photoreduction of nitrobenzene over visible-light-driven $PtO@Cr_2O_3$ nanocomposites[J]. Surf Interfaces, 27: 101527.

JIANG L, SUN G, ZHOU Z, et al, 2005. Size-controllable synthesis of monodispersed SnO_2 nanoparticles and application in electrocatalysts[J]. J Phys Chem B, 109(18): 8774-8778.

KERTALLI E, SCHOUTEN J C, NIJHUIS T A, 2017. Effect of hydrogen and propylene on the hydrogen peroxide decomposition over Pt, PtO and Au catalysts [J]. Appl Catal A Gen, 538: 131-138.

LEE G, SHIM J H, KANG H, et al, 2009. Monodisperse Pt and $PtRu/C_{60}$ hybrid nanoparticles for fuel cell anode catalysts [J]. Chem Commun, (33): 5036-5038.

LI F, CAO B, ZHU W, et al, 2017. Hydrogenation of phenol over Pt/CNTs: The effects of Pt loading and reaction solvents[J]. Catalysts, 7(5): 145.

LI W, XIAN L, ZHAO Y, et al, 2023. Stepwise preparation of uniform-size ultrafine Pt nanoparticles for high-performance catalysis of methanol oxidation and nitrophenol reduction [J]. ACS Appl Nano Mater, 6(20): 19176-19188.

LI Y, CAO Y, XIE J, et al, 2015. Facile solid-state synthesis of Ag/graphene oxide nanocomposites as highly active and stable catalyst for the reduction of 4-nitrophenol[J]. Catal Commun, 58: 21-25.

LIU P, ZHAO Y, QIN R, et al, 2016. Photochemical route for synthesizing atomically dispersed palladium catalysts[J]. Science, 352(6287): 797-801.

MA J, HABRIOUX A, PISAREK M, et al, 2013. Induced electronic modification of Pt nanoparticles deposited onto graphitic domains of carbon materials by UV irradiation[J]. Electrochem Commun, 29: 12-16.

MAO J, CHEN Y, PEI J, et al, 2016. Pt–M (M = Cu, Fe, Zn, etc.) bimetallic nanomaterials with abundant surface defects and robust catalytic properties[J]. Chem Commun, 52(35): 5985-5988.

NIE R, WANG J, WANG L, et al, 2012. Platinum supported on reduced graphene oxide as a catalyst for hydrogenation of nitroarenes[J]. Carbon, 50(2): 586-596.

ORTIZ-HERRERA J C, CRUZ-MARTÍNEZ H, SOLORZA-FERIA O, et al, 2022. Recent progress in carbon nanotubes support materials for Pt-based cathode catalysts in PEM fuel cells[J]. Int J Hydrog Energy, 47(70): 30213-30224.

PANIGRAHI S, BASU S, PRAHARAJ S, et al, 2007. Synthesis and size-selective catalysis by supported gold nanoparticles: Study on heterogeneous and homogeneous catalytic process[J]. J Phys Chem C, 111(12): 4596-4605.

RANJANA M, SAHU P, RAMESH V V E, et al, 2023. Ethylenediamine mediated, environmentally benign synthesis of copper nanowires and their catalytic activity towards 4-nitrophenol reduction[J]. ChemistrySelect, 8(30): e202204351.

SANTIAGO E I, VARANDA L C, VILLULLAS H M, 2007. Carbon-supported Pt-Co catalysts prepared by a modified polyol process as cathodes for PEM fuel cells[J]. J Phys Chem C, 111(7): 3146-3151.

SHI W, ZHANG B, LIN Y, et al, 2016. Enhanced chemoselective hydrogenation through tuning the interaction between Pt nanoparticles and carbon supports: Insights from identical location transmission electron microscopy and X-ray photoelectron spectroscopy[J]. ACS Catal, 6(11): 7844-7854.

SHI Y C, FENG J J, LIN X X, et al, 2019. One-step hydrothermal synthesis of three-dimensional nitrogen-doped reduced graphene oxide hydrogels anchored PtPd alloyed nanoparticles for ethylene glycol oxidation and hydrogen evolution reactions [J]. Electrochim Acta, 293: 504-513.

SONG P T, 2022. Finite-size effect of a weakly interacting Bose gas at zero-temperature[J]. Phys Lett A, 455: 128515.

SUBHAN F, ASLAM S, YAN Z, et al, 2021. Palladium nanoparticles decorated on ZSM-5 derived micro-/ mesostructures (MMZ) for nitrophenol reduction and MB degradation in water[J]. J Environ Chem Eng, 9(1): 105002.

SUN X Q, GAO X H, WANG Y Y, et al, 2022. Study of the mechanism of nitrogen doping in carbon supports on promoting electrocatalytic oxygen reduction reaction over platinum nanoparticles [J]. J Fuel Chem Technol, 50(11): 1427-1436.

SWAIN S，ALTAEE A，SAXENA M，et al，2022. A comprehensive study on heterogeneous single atom catalysis：Current progress，and challenges[J]. Coord Chem Rev，470：214710.

TOL R T，MATHOT V B F，GROENINCKX G，2005. Confined crystallization phenomena in immiscible polymer blends with dispersed micro- and nanometer sized PA6 droplets，part 2：Reactively compatibilized PS/PA6 and（PPE/PS）/PA6 blends[J]. Polymer，46(2)：383-396.

TUO Y X，SHI L J，CHENG H Y，et al，2018. Insight into the support effect on the particle size effect of Pt/C catalysts in dehydrogenation[J]. J Catal，360：175-186.

XIAN L，MA J，LI W，et al，2022. Synthesis of ultrafine platinum nanocatalysts by ice-photochemical method and their application in catalytic degradation of 4-nitrophenol[J]. ChemistrySelect，7(45)：e202204071.

XIAN L，SU B Q，FENG Y X，et al，2021. The photochemical effects of visible light on $K_2[PtCl_4]$ hydrolysis and the synthesis of Pt nano catalysts[J]. Inorg Nano Met Chem，51(6)：882-888.

XIANG Y Z，LV Y A，XU T Y，et al，2011. Selectivity difference between hydrogenation of acetophenone over CNTs and ACs supported Pd catalysts[J]. J Mol Catal A Chem，351：70-75.

XIE W，ZHANG Y，LIEW K，et al，2012. Effect of catalyst confinement and pore size on Fischer-Tropsch synthesis over cobalt supported on carbon nanotubes[J]. Sci China Chem，55(9)：1811-1818.

XUE H，ZHANG J，HAN S，et al，2019. Effect of asphaltenes on the structure and surface properties of wax crystals in waxy oils[J]. Energy Fuels，33(10)：9570-9584.

YANG F R，GAO L，LAI W C，et al，2023. Recent advance on structural design of high-performance Pt-based nanocatalysts for oxygen reduction reaction[J]. Adv Sens Energy Mater，2(1)：100022.

YOO P K，KIM S，2022. Preparation and electrochemical activity of platinum catalyst-supported graphene and Fe-based metal-organic framework composite electrodes for fuel cells[J]. J Ind Eng Chem，105：259-267.

ZHANG M，LIU J，ZHANG Y H，et al，2023a. Preparation of highly dispersed silicon spheres supported cobalt-based catalysts and their catalytic performance for Fischer-Tropsch synthesis[J]. J Fuel Chem Technol，51(5)：608-615.

ZHANG Q，LU X，YUE F，et al，2023b. N-doped semi-graphitic C loaded with metallic Co：Synthesis parameters and catalytic selective reduction of *p*-nitrophenol[J]. New J Chem，47(8)：3834-3846.

ZHAO J，CHEN C，MA W，2005. Photocatalytic degradation of organic pollutants under visible light irradiation[J]. Top Catal，35(3)：269-278.

ZHAO Z，BAI P，DU W，et al，2020. An overview of graphene and its derivatives reinforced metal matrix composites：Preparation，properties and applications[J]. Carbon，170：302-326.

ZHOU C，GAN M，XIE F，et al，2020. Pt nanoparticles coated on multiwalled carbon nanotubes by the modification of small-sized molybdenum phosphide for enhanced methanol electro-oxidation[J]. Ionics，26(12)：6331-6340.

ZHOU X，BAI X，2023. PdCu alloy prepared by ultrasonic method catalyzes the degradation of p-nitrophenol[J]. Environ Sci Pollut Res，30(16)：48449-48459.

ZHU J，FIGUEIREDO J L，FARIA J L，2008. Au/activated-carbon catalysts for selective oxidation of alcohols with molecular oxygen under atmospheric pressure：Role of basicity[J]. Catal Commun，9(14)：2395-2397.

超细铂纳米催化剂的光化学合成及其催化还原硝基苯酚的应用

鲜亮[1,2]，田小霞[1]，马婧[1]，李伟[1]

1. 西北民族大学化工学院，甘肃 兰州 730030
2. 甘肃省高校环境友好复合材料及生物质利用省级重点实验室，甘肃 兰州 730030

摘要： 以乙二醇（EG）为还原剂，通过波长为 395 nm 近紫外光和 450、650 nm 的可见光照射 C_{60} 及 $K_2[PtCl_4]$ 混合液，制备了超细铂纳米颗粒（Pt/C_{60}-E）。利用 X 射线衍射（XRD）、傅里叶变换红外光谱（FT-IR）、X 射线光电子能谱（XPS）以及高分辨率透射电子显微镜（HR-TEM）等表征手段对 Pt/C_{60} 催化剂的组成及形貌进行了研究，结果表明，铂纳米颗粒在 C_{60} 表面分散良好，平均粒径约为 2.6 nm。在催化 *p*-NP 还原实验中，在近紫外光（395 nm）照射下所制备催化剂（Pt/C_{60}-E3）表现出最高的催化活性，其速率常数 k=0.12 min^{-1}。在催化剂循环实验中，多次循环催化剂仍具有较高的活性，实验证明光化学法对前驱体铂催化剂制备起到良好的作用。

关键词： 超细铂纳米颗粒；富勒烯；光化学法；降解 *p*-硝基苯酚

（责任编辑　张　冰）